Structural basis for higher-order DNA binding by a bacterial transcriptional regulator

Frederik Oskar Graversgaard Henriksen[1], Lan Bich Van[1], Ditlev Egeskov Brodersen[1], and Ragnhild Bager Skjerning[1]*

[1]Department of Molecular Biology and Genetics, Universitetsbyen 81, Aarhus University, DK-8000 Aarhus C, Denmark, [*]To whom correspondence should be addressed (raba@mbg.au.dk)

ABSTRACT

Transcriptional regulation by binding of transcription factors to palindromic sequences in promoter regions is a fundamental process in bacteria. Some transcription factors have multiple dimeric DNA-binding domains, in principle enabling interaction with higher-order DNA structures; however, mechanistic and structural insights into this phenomenon remain limited. The *Pseudomonas putida* toxin-antitoxin (TA) system Xre-RES has an unusual 4:2 stoichiometry including two potential DNA-binding sites, compatible with a complex mechanism of transcriptional autoregulation. Here, we show that the Xre-RES complex interacts specifically with a palindromic DNA repeat in the promoter in a 1:1 molar ratio, leading to transcriptional repression. We determine the 2.7 Å crystal structure of the protein-DNA complex, revealing an unexpected asymmetry in the interaction and suggesting the presence of a secondary binding site, which is supported by structural prediction of the binding to the intact promoter region. Additionally, we show that the antitoxin can be partially dislodged from the Xre-RES complex, resulting in Xre monomers and a 2:2 Xre-RES complex, neither of which repress transcription. These findings highlight a dynamic, concentration-dependent model of transcriptional autoregulation, in which the Xre-RES complex transitions between a non-binding (2:2) and a DNA-binding (4:2) form.

KEYWORDS

Crystal structure, HTH domain, RES toxin, Toxin-antitoxin, Transcriptional regulation

AUTHOR SUMMARY

Bacteria regulate their gene expression to respond to environmental stress, to evade antibiotics, and to maintain population stability. In this study, we investigate how the *xre-res* toxin-antitoxin system from *Pseudomonas putida* controls its own expression. Using a combination of microbiology,

structural biology, biophysical assays, and computational modelling, we discover how the Xre-RES protein complex represses its own transcription through direct binding to a specific DNA element in the promoter region. We show structurally that the Xre-RES complex adopts a unique 4:2 stoichiometry and binds DNA in an unusual asymmetrical manner. Moreover, the complex was found to shift between two different forms: one that binds DNA and represses transcription, and one that does not. We further demonstrate that this shift is dynamic and depends on the relative concentration of Xre antitoxin. Our findings provide new insight into how bacteria fine-tune gene expression and offers a model of transcriptional control based on protein stoichiometry and structural asymmetry.

INTRODUCTION

Regulation of transcription is a fundamental mechanism in bacteria that allows adaptation to constantly changing environments, and RNA polymerase (RNAP) plays a central part in this. The core RNAP enzyme has a $\beta\beta'\alpha_2$ subunit composition [1] but in order to form a holoenzyme and initiate transcription at a particular promoter, the core enzyme needs to interact with a σ subunit [2, 3]. The σ subunit ensures promoter recognition and positioning of the RNAP holoenzyme at the promoter and unwinding of the DNA duplex near the transcriptional start site (TSS). Transcriptional activity can be modulated by repressor proteins that bind directly to a segment of the promoter (the operator) and inhibits transcription [4]. Repression can occur by one of three mechanisms: steric hindrance of RNAP binding to the promoter, interference with post-recruitment steps in transcriptional initiation such as the assembly of the RNAP holoenzyme, or DNA looping upon repressor binding [1]. A common feature of many repressor proteins is the presence of a DNA-binding helix-turn-helix (HTH) domain [5]. The generic HTH domain is a simple fold comprised of three core helices of which the second and third helix are connected by a sharp turn and makes up

64 the HTH motif [5, 6]. The third helix is also called the 'recognition helix' and usually recognizes a
65 symmetrical sequence element in the DNA by inserting directly into the major groove [7]. The
66 binding efficiency a repressor protein to an operator site depends on its binding affinity, which
67 again is determined by base-specific readouts and intrinsic DNA shape, however, in many cases, the
68 mechanism by with repressor proteins recognise DNA *in vivo* remains unclear [8-10].
69
70 Due to the symmetrical nature of DNA, most HTH-containing protein repressors are functional as
71 dimers, which sometimes depend on even higher-order structures and additional proteins. Thus,
72 HTH domains often bind palindromic DNA sequences separated by approximately a single helical
73 turn, allowing for the recognition helices to insert into adjacent major grooves [7]. In the
74 widespread *xre-res* system [11], the encoded Xre (Xenobiotic response element) protein contains a
75 putative HTH DNA-binding domain that is stabilised in a higher-order structure through interaction
76 with the associated RES-domain protein [12-14]. The two proteins are expressed from two-gene
77 operons that have been classified as toxin-antitoxin (TA) systems, which are widely distributed
78 cellular regulators in bacteria that encode a protein toxin that inhibits cell growth along with a
79 cognate protein antitoxin that neutralises it [15]. The RES toxin has an ADP-ribosyltransferase
80 fold and expression of an orthologue from the insect pathogen, *Photorhabdus luminescens*,
81 has been shown to result in efficient depletion of intracellular NAD^+ in *E. coli*, suggesting that
82 the RES toxin is a NAD^+ glycohydrolase (NADase). Similar results were obtained for the RES-
83 domain toxins MbcT from *Mycobacterium tuberculosis* [12], SlvT from *P. putida* S12 [16],
84 PA14_51010 from *P. aeruginosa* PA14 [17], and VPA0770 from *Vibrio parahaemolyticus* [18],
85 while PrsT from *Sinorhizobium meliloti* toxin is structurally similar appears to function as an ADP
86 ribosyltransferase (mART) targeting and inactivating phosphoribosyl pyrophosphate synthetase
87 (Prs) [13]. The role of RES domain-containing TA systems in bacterial cell biology is still largely

88 unknown, but a recent study showed that the *P. aeruginosa* orthologue, PA14_51010 (NatT),
89 mediates NAD^+ depletion leading to drug-tolerant dormant cell populations *in vitro* and suggesting
90 that the accumulation of NatT-activating mutations observed during *P. aeruginosa* infections in
91 human cystic fibrosis patients increases antibiotic tolerance [19].
92
93 The crystal structure of a Xre-RES complex from *Pseudomonas putida* revealed an unusual 4:2 TA
94 stoichiometry in which each of the RES domains of a central toxin dimer interacts with a dimer of
95 Xre antitoxins, thus generating two complete HTH domains [14]. The HTH domain of this Xre
96 antitoxin (Xre^{Pp}) is structurally similar to the bacteriophage lambda Cro repressor [20] and could
97 thus potentially play a part in transcriptional regulation and toxin control through binding of
98 the antitoxin to the TA promoter region, as observed for many TA systems [21]. For some of
99 these, the presence of the toxin only stabilises the interaction with DNA up to a certain level
100 after which a higher stoichiometry of toxin molecules leads to de-repression by a mechanism
101 termed *conditional cooperativity* [22-24]. However, other modes of autoregulation exist,
102 including via recruitment of external regulators, three-component TA systems in which the
103 DNA binding domain is present in a third protein separate from the antitoxin, and TA
104 modules with reversed gene order and multiple promoter sites [25]. The observation that the
105 *P. putida* Xre-RES complex contains two complete DNA-binding domains each composed by
106 two HTH domains suggests the system may be regulated in a novel way. However, the
107 organisation of the promoter region and the mechanism of DNA binding and transcriptional
108 regulation are currently unknown.
109
110 In this paper, we dissect the mechanism of transcriptional autoregulation of the *P. putida xre-res*
111 system. Our findings reveal that a Xre–RES^{Pp} complex with 4:2 stoichiometry binds in a 1:1 ratio to

112 an imperfect inverted repeat region in the promoter region and effectively represses transcription.
113 We determine a 2.7 Å crystal structure of the Xre-RES^{Pp} complex bound to the imperfect inverted
114 repeat, showing that the interaction is unusually asymmetric. Moreover, interactions to one end of a
115 symmetry-related DNA-duplex suggests a second binding site in the operator region, which is
116 supported by structure prediction of the interaction to the intact promoter DNA sequence. Finally,
117 we show that the isolated Xre^{Pp} antitoxin is a monomer that only weakly represses the promoter.
118 Surprisingly, individual Xre^{Pp} monomers can dislodge from the 4:2 complex, resulting in a 2:2
119 complex incapable of binding DNA. Together, our data provides a model for how the Xre-RES^{Pp}
120 complex autoregulates transcription through a balance between binding and non-binding forms,
121 driven by protein stoichiometry and asymmetry as well as general insights into interaction of
122 transcription factors with higher-order DNA in bacteria.
123

124 **RESULTS**

125 **The *P. putida xre-res* locus is transcriptionally auto-regulated**

126 The presence of a DNA-binding HTH domain in Xre^{Pp} suggested that the antitoxin and/or the Xre-
127 RES TA complex could be involved in regulating transcription of the *P. putida xre-res* operon via
128 direct promoter binding. To test this hypothesis, we analysed the *xre-res*^{Pp} promoter region (P_{XR})
129 and identified three inverted repeats and one directional repeat (named S1-S4, **Fig 1A and Fig**
130 **S1A**). To investigate the promoter activity *in vivo*, we constructed a low-copy GFP reporter plasmid
131 (pGH254Kgfp) containing the intact P_{XR} promoter region, including the 5' end (30 bp) of *xre*^{Pp},
132 transcriptionally fused to *gfpmut2* encoding a Green Fluorescent Protein (GFP) variant
133 (S65A/V68L/S72A) with enhanced fluorescence emission and more efficient folding at 37°C as
134 compared to the wild type GFP [26]. The resulting construct, as well as a plasmid expressing *xre-*
135 *res*^{Pp} under arabinose-inducible control, was introduced into *E. coli* MG1655 by transformation,

136 and the GFP signal monitored throughout growth in the presence or absence of arabinose (**Fig 1B**).

137 The results show that the P_{XR} promoter is active in *E. coli* during exponential growth (**Fig 1C**).

138 Moreover, induction of *xre-res*^{Pp} in this background results in complete absence of GFP signal (**Fig.**

139 **1D**, orange curve) compared to the strain containing an empty pBAD33 vector (**Fig. 1D**, green

140 curve). Together, this supports that *xre-res*^{Pp} negatively regulates expression from P_{XR}.

141

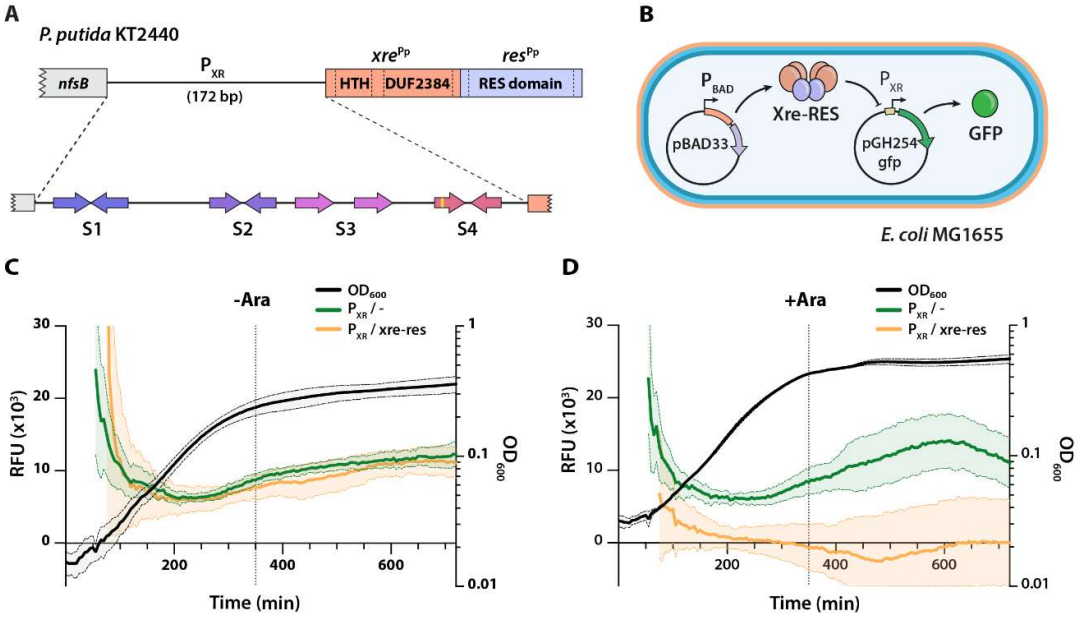

142
143 **Figure 1. Organisation, activity, and regulation of the *xre-res*^{Pp} operon**.
144 (A) Schematic representation the *P. putida* KT2440 *xre-res*^{Pp} locus including the 172-bp promoter region
145 (P_{XR}) and the upstream gene (*nfsB*). Top, the *xre*^{Pp} gene (orange) encodes a protein antitoxin with an N-
146 terminal helix-turn-helix (HTH) domain and a C-terminal domain of unknown function (DUF2384), known
147 to interact with the RES toxin, while *res*^{Pp} (blue) encodes a NADase toxin with a RES domain. Below,
148 close-up of the P_{XR} promoter region showing the three inverted repeats (S1, S2, and S4) and one directional
149 repeat (S3), of which S4 is imperfect and contains one mismatch (yellow box, see also **Fig S1A**). (B)
150 Overview of the GFP-based assay to measure regulation of P_{XR} in *E. coli* MG1655 *in vivo*. The pBAD33
151 vector allows for arabinose induction of the *xre-res*^{Pp} genes while P_{XR} coupled to GFP allows for read-out
152 of the transcriptional activity of the promoter. (C) and (D) Promoter activity assays in *E. coli* MG1655.
153 Activity is measured as GFP signal in relative fluorescence units (RFU) during growth without ((C), -Ara)
154 or with ((D), +Ara) arabinose using the promoter reporter pGH254Kgfp::P_{XR} (P_{XR}), as well as empty
155 pBAD33 (-, green curves) or pBAD33::*xre-res*^{Pp} vector (*xre-res*, orange curves). All curves represent mean-
156 of-mean values (line, n = 3) with standard error of mean (SEM) shown as a shadow. The dotted vertical
157 line indicates the 350 min time point
158

159 **Expression of *xre-res*^{Pp} represses promoter activity via an imperfect repeat upstream of *xre*^{Pp}**

160 To determine the minimal promoter requirements for active transcription from the *xre-res*^{Pp} locus,
161 we repeated the assay using variants of P_{XR} where one or more of the four identified repeats (S1-S4)
162 were systematically removed (**Fig 2A** and **S1 Table**). To simplify the comparison and since the P_{XR}
163 promoter was found to be most active during late exponential growth, the GFP fluorescence level
164 measured at t=350 min was used for this analysis (complete curves are included in **Fig S1** and **S2**).
165 Removal of S1 (ΔS1) did neither affect promoter activity nor repression by *xre-res*^{Pp}, while removal
166 of both S1 and S2 (ΔS1-S2), resulted in significantly increased promoter activity that can still be
167 fully repressed by *xre-res*^{Pp} (**Fig 2B**). In contrast, removal of either S1 through S3 (ΔS1-S3), S3 and
168 S4 (ΔS3-4), or just S4 (Δ4), completely abolished transcription (**Fig 2B**). Interestingly, removal of
169 only the central palindromic part of the imperfect inverted repeat in S4 (Δrepeat, **Fig 2C** and **S1**
170 **Table**) did not affect promoter activity while expression of *xre-res*^{Pp} only weakly (and non-
171 significantly) repressed transcription of this variant (**Fig 2D**). Together, this suggests that
172 transcriptional control by *xre-res*^{Pp} depends on the imperfect inverted repeat in the S4 region while
173 transcription does not. To investigate the importance of the imperfect part of the inverted repeat, we
174 created two variants with perfect repeats by either introducing G->T on the coding strand in the first
175 half of the repeat (5'-perf) or A->C in the second half of the repeat (3'-perf) (**Fig 2C** and **S1 Table**).
176 Both substitutions decreased promoter activity as compared to wild type but did not affect the
177 ability of *xre-res*^{Pp} to repress transcription, suggesting that the imperfectness of the inverted repeat
178 is required for optimal transcription but not repression (**Fig 2D**).
179

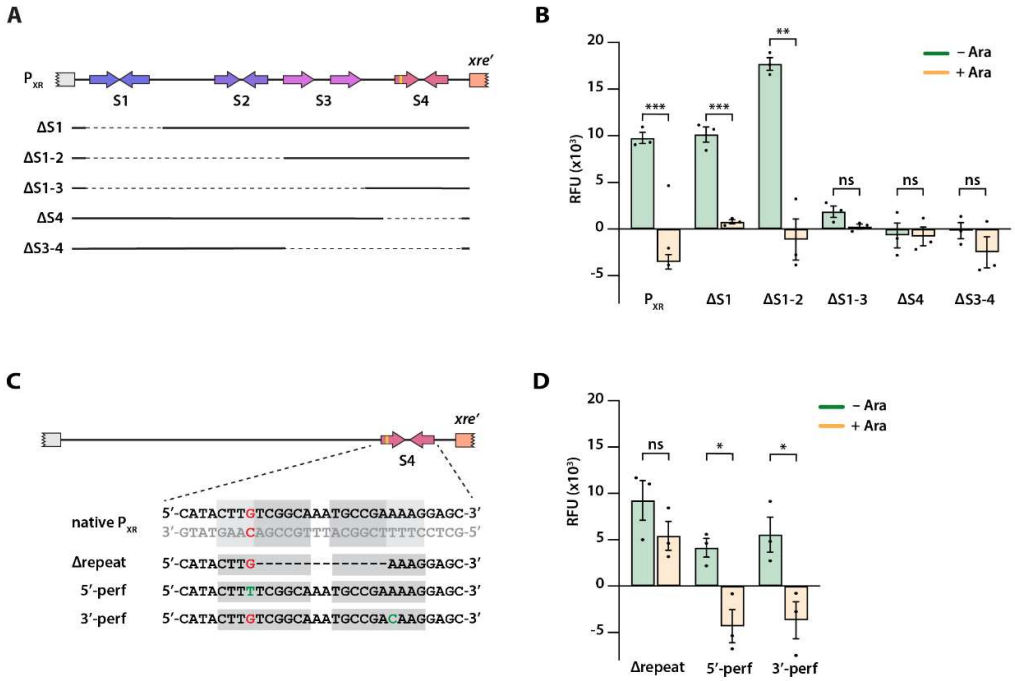

Fig 2. Determination of the minimal promoter requirements for transcription and regulation of P_{XR}. (A) Detailed overview of the P_{XR} promoter (top) and schematic representation of promoter variants (below). Full lines indicate the included parts while dotted lines represent regions that have been removed. Complete growth curves and details of the constructs are found in **Fig S1** and **S1 Table**. (B) Promoter activity assays in *E. coli* MG1655. The reporter plasmid pGH254Kgfp encoding promoter variations was combined with pBAD33::*xre-res*^{Pp}. For each variant, the GFP signal (RFU) measured at t=350 min from non-induced cultures (-Ara, green bars) is compared to that from arabinose-induced cultures (+Ara, orange bars). Mean RFU values extracted at the same time point from three independent experiments were treated as biological replicates (dots, $n = 3$) and error bars show SEM. Complete growth curves are included in **Fig S1**. Statistical analysis was performed using two-way analysis of variance (ANOVA) followed by Dunnett's multiple comparisons test. *ns*, not significant; ***, $p < 0.01$; ****, $p < 0.0001$. (C) Schematic representation of the repeat variants of the imperfect inverted repeat in S4 of the P_{XR} promoter region. The DNA sequence of the imperfect inverted repeat is highlighted (light grey), including the mismatch in the first repeat (red), the perfect part of the repeat (dark grey) and the alterations (green). The mismatch was removed by a substitution either in the first (5'-perf) or second (3'-perf) half of the repeat. (D) As b, but using promoter variations from c. *ns*, not significant; *, $p < 0.05$; **, $p < 0.01$.

The Xre-RES^{Pp} complex binds directly to S4 *in vitro*

The presence of an HTH domain in Xre and the observed repression of transcription upon expression of *xre-res*^{Pp} indicated that the Xre-RES^{Pp} protein complex might bind directly to DNA. To investigate this, we analysed the binding between the Xre-RES^{Pp} protein complex and different parts of the P_{XR} promoter *in vitro*. First, we expressed and purified the intact Xre-RES^{Pp} complex via a N-terminal His_6-tag on the RES toxin (Xre-RES$^{Pp}_{His6}$) and used size exclusion chromatography coupled to multi-angle light scattering (SEC-MALS) to show that Xre and RES_{His6}

205 form a protein complex with an estimated MW of 92 ± 4 kDa (**Fig 3A**), which best matches the
206 theoretical mass of the 4:2 Xre-RES complex of approximately 103 kDa observed in the crystal
207 structure (**Fig 3B**) [14]. We then analysed the ability of the purified complex to bind a set of 30 bp
208 dsDNA probes each covering one of the four sequence elements (S1 to S4) in the P_{XR} promoter (**Fig**
209 **1A** and **Fig S1A**). For this, purified Xre-$RES^{Pp}{}_{His6}$ complex and dsDNA probes were incubated in
210 1:1 molar ratio followed by analytical SEC (a-SEC). A significant change in elution volume of 0.2
211 mL and a concomitant change in the 260:280 nm absorbance ratio from 0.54 to 0.68 was observed
212 for complex mixed with S4 dsDNA (**Fig 3C**), but not for S1, S2 or S3 dsDNA (**Fig S3A-C**),
213 suggesting that the Xre-RES^{Pp} complex binds specifically to the S4 element of the P_{XR} promoter.
214
215 Previously, structure determination of the Xre-RES^{Pp} complex has shown that the 4:2
216 heterohexamer contains two complete Cro-like Xre^{Pp} dimers [14], each potentially capable of
217 binding dsDNA via interaction with adjacent major grooves [27]. To investigate whether the S4
218 element is the only binding site in the promoter, we determined the binding stoichiometry by
219 analysing the binding at different protein:DNA ratios using SEC-MALS. At a 1:1 ratio of Xre-
220 RES^{Pp} complex to dsDNA duplex, and thus a ratio of putative binding sites to DNA of 2:1, we
221 found that the protein complex was unable to bind all DNA present in solution (**Fig S3D**), and
222 increasing this to a 1:2 ratio of protein complex to DNA, no additional shift in the elution volume or
223 calculated mass was observed as compared to the 1:1 ratio (**Fig S3D**). To further probe the
224 stoichiometry of binding between the Xre-RES^{Pp} complex and S4 dsDNA, we saturated the protein
225 complex with increasing amounts of DNA and used high-resolution SEC (2.4 mL) to check for
226 indication of a second DNA binding site. Even at a molar ratio of protein complex to dsDNA of
227 1:10, only a marginal shift in the elution volume of 0.01 ml (0.6% CV) was observed (**Fig S3E**).
228 Together, this suggests that the 4:2 Xre-RES^{Pp} complex only binds a single copy of S4 dsDNA. To

229 further quantify the binding interaction between the Xre-RES^{Pp} complex and S4, we determined the
230 binding coefficient (K_D) using isothermal titration calorimetry (ITC). This showed that the Xre-
231 RES^{Pp} complex binds with a 1:1 ratio and high affinity to the native S4 element (K_D = 231 ± 46 nM,
232 **Fig 3D**), while the affinities towards both the 5'-perf (K_D = 341 ± 264 μM) and 3'-perf variants (K_D
233 = 80 ± 79 μM) of S4 were drastically reduced (**Table 2**). Given that repression by *xre-res^{Pp}* is intact
234 for these two variants (5'-perf and 3'-perf) *in vivo*, these data are consistent with the existence of a
235 second DNA binding site that strengthens the protein-DNA interaction in the context of the full-
236 length promoter.
237

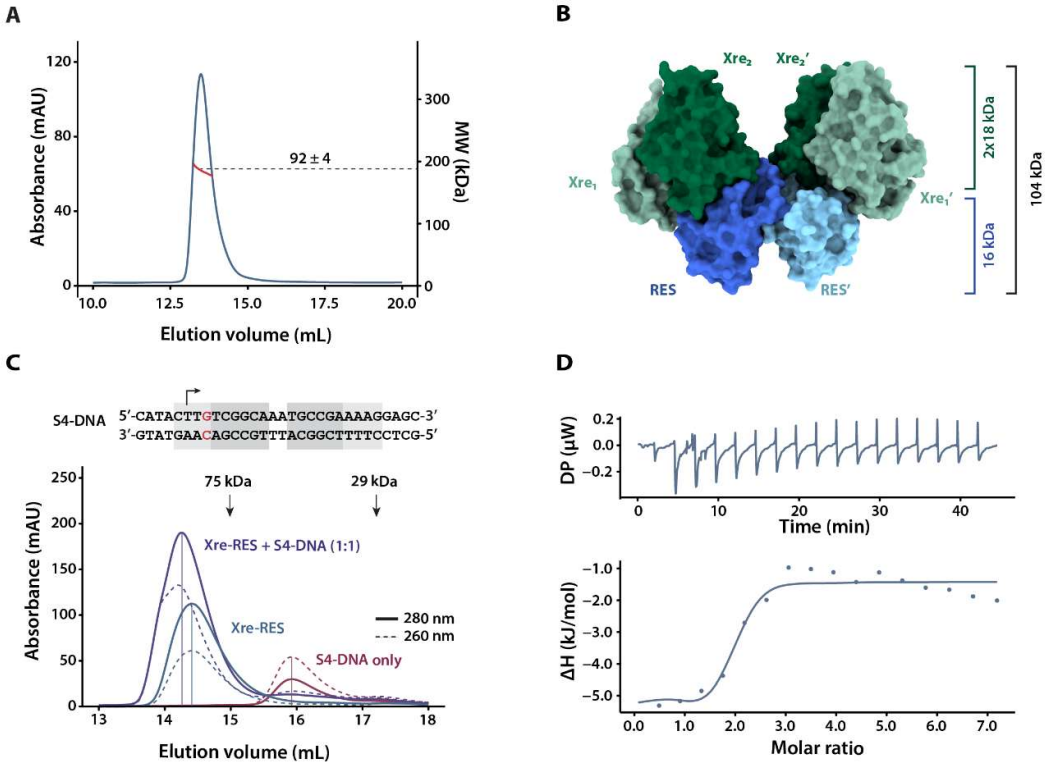

238
239 **Figure 3. Xre-RES^{Pp} forms a 4:2 hexameric complex in solution and interacts specifically with the S4**
240 **element of the promoter.**
241 (A) SEC-MALS analysis of purified Xre-RES$^{Pp}{}_{His6}$ complex. The chromatogram shows the elution profile
242 as measured by absorption at 280 nm (blue) and the molecular mass measured by MALS (red). The average
243 mass corresponding to the middle of the peak is 92 ± 4 kDa (dotted line). (B) The crystal structure of
244 heterohexameric Xre-RES^{Pp} (PDB: 6GW6) with total mass (103 kDa) and HTH domains indicated [14].
245 The RES toxins are coloured in shades of blue, while the Xre antitoxins are in shades of green. (C)
246 Analytical SEC (a-SEC) analysis of Xre-RES$^{Pp}{}_{His6}$ (Xre-RES, blue), S4 (S4-DNA only, red), and DNA
247 mixed with protein in a 1:1 ratio (Xre-RES + S4-DNA, purple). Black arrows represent known molecular

weight standards (conalbumin, 75 kDa; carbonic anhydrase, 29 kDa). The full line shows 280 nm absorbance, while the dotted line is 260 nm absorbance. (D) Isothermal Titration Calorimetry (ITC) titration of S4 dsDNA into the Xre-RES^{Pp} complex. The top panel shows the raw thermogram (DP, differential power), while the bottom panel shows the integrated heat per injection (ΔH, kJ/mol), the solid is line is the fit using the "one set of sites" model.

The structure of the Xre-RES^{Pp}-DNA complex reveals an unusual, asymmetrical DNA binding site

To get a molecular understanding of the interaction between Xre-RES^{Pp} and promoter DNA, we determined the crystal structure of the Xre-RES^{Pp} complex bound to a 30 bp dsDNA oligo covering the S4 element to 2.7 Å (R / R_{free} = 22.8% / 26.9%, **Fig 4A, Table 1**). The structure contains four complete heterohexameric (4:2) Xre-RES^{Pp} complexes and four DNA duplexes in the crystallographic asymmetric unit (**Fig S4A**). In all molecules, one Xre dimer of each Xre-RES^{Pp} complex interacts strongly with two adjacent major grooves on dsDNA (**Fig 4A** and **Fig S4B**). The interaction between the Xre dimer and DNA causes the major groove on the opposing side of the double helix to expand from 11.8 Å in canonical B-DNA to 14 Å (**Fig 4A**). Significantly, we observe that the Xre dimer is asymmetrical in the way it interacts with DNA and overall approaches the double helix in a different way than classical HTH domains such as the Cro-repressor [28]. More specifically, the angle between the helical axis of DNA and that of the recognition helix of the outer Xre molecule is 61.4° while it is 57.5° for the inner Xre molecule. These values are both significantly smaller and more different from each other than observed for the canonical structure of the Cro repressor bound to DNA (PDB 1RPE), in which the the two recognition helices of the Cro dimer approach DNA at nearly identical angles of 68.8° **(Fig S4C**) (Shimon & Harrison, 1993). Several residues in Xre, in particular Arg60, Arg67, Thr68, Lys70, and Arg72, interact tightly with C13, C20, and G21 on the (+) strand, as well as T7, T8, T9, and A14 on the (-) strand of S4 DNA (**Fig 4B** and **4C**). The dominant interactions are centred around the conserved Arg67 of the innermost Xre, which engages in hydrogen bonds to the N3 atom of T9 of the DNA (-) strand (**Fig**

276 **4C**). Interestingly, Arg67 of the outermost Xre displaces A14 of the (+) strand and forms hydrogen
277 bonds to the N3 of C13 (+) (**Fig 4C**). Arg60, Thr68, Lys70, and Arg72 also make non-sequence
278 specific interactions to the phosphodiester backbone of DNA. Of the interacting residues, both
279 Thr68 and Arg72 are functionally conserved across *xre-res* loci from a wide range of bacterial
280 species, while Arg67 and Lys70 appear conserved in a subset of species (**Fig 4D**). To support the
281 importance of Arg67 in DNA binding by Xre, we substituted this residue with alanine (R67A) and
282 found that transcriptional repression by *xre*^{R67A}*-res in vivo* was abolished (**Fig 4E** and **Fig S4D**).

283 Intriguingly, inspection of the second Xre dimer of the Xre-RES heterohexamer reveals that there
284 are interactions to one end of a DNA duplex from a symmetry-related complex (**Fig 4F**). The
285 specific interactions made at this site vary slightly between complexes in the asymmetric unit but in
286 all cases include base-specific interactions between Arg67 of the outermost Xre molecule to O2 on
287 T7 on the (+) strand, and non-sequence specific interactions between Thr68 and Ser71 to the
288 backbone of A4 and C5 of the (+) strand as well as between Arg75 and Gln77 and C19 of the (-)
289 strand (**Fig 4B**). In summary, the structure of DNA-bound Xre-RES^{Pp} confirms that one of the two
290 Xre dimers in the complex recognises S4 dsDNA using base-specific interactions dependent on
291 Arg67 and moreover, that the second Xre dimer is capable of simultaneously interacting with DNA
292 supporting the idea that there might be a secondary DNA binding site inside the full operator
293 region.

294

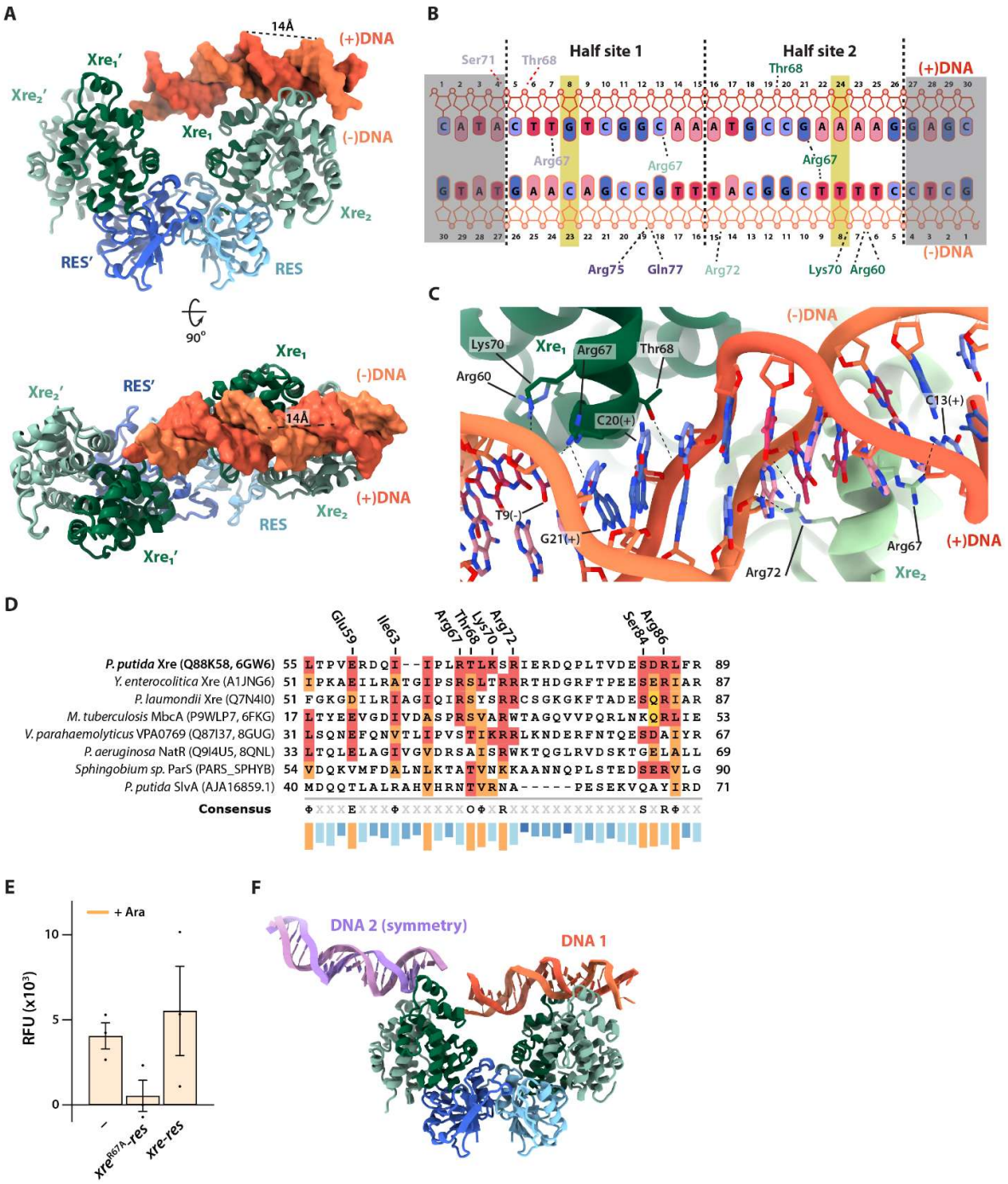

Figure 4. Crystal structure of the DNA-bound Xre-RES^{Pp} complex.
(A) Overview of the *P. putida* Xre-RES complex (green/blue cartoon) is bound to a 30 bp dsDNA (red/orange) with both HTH recognition helices of the of a single Xre dimer interacting with DNA. (B) Schematic overview of the interactions between Xre and DNA including both sequence specific and unspecific contacts as well as the contacts from the symmetry related interaction. The shaded DNA region could not build. (C) Close-up on the interaction between Xre and DNA with interactions between selected residues of both Xre molecules and the DNA highlighted. (D) Sequence alignment of *P. putida* Xre and a range of homologous proteins from other bacterial species. UniProt IDs are listed in parentheses for all proteins, together with and PDB IDs for *P. putida* Xre (PDB ID 6GW6) [14], *M. tuberculosis* MbcA (PDB

ID 6FKG) [12], *V. parahaemolyticus* (PDB ID 8GUG) [18], and *P. aeruginosa* NatR (PDB ID 8QNL) [19]. Residues conserved with *P. putida* Xre are shown in red with functionally similar residues in orange. Starting and ending residue numbers are listed at each end of the sequences. (E) Promoter activity in *E. coli* MG1655 for promoter reporter plasmid pGH254Kgfp::P_{XR} (P_{XR}) in combination with pBAD33 (-), pBAD33::*xre*^{R67A}-*res*^{Pp} (*xre*^{R67A}-*res*), or pBAD33::*xre-res*^{Pp} (*xre-res*), as indicated. Complete growth curves and details of the constructs are found in **Fig S4**. (F) In the crystal, the Xre-RES complex (blue/green) interacts with a primary dsDNA molecule (DNA 1) as well as a symmetry-related DNA molecule (DNA 2).

The Xre^{Pp} dimer is stabilised by higher-order complex formation and required for transcriptional repression

Since the structure shows that only one of the two Xre dimers in the complex is bound to S4 dsDNA, we speculated whether Xre alone can repress transcription. To investigate this, we used the transcriptional coupling to GFP during to compare the activity of the wild type P_{XR} promoter during induction of either *xre*^{Pp} or *xre-res*^{Pp}. While expression of the complex fully repressed transcription as seen before, expression of *xre*^{Pp} alone only partially, and not significantly, repressed transcription (**Fig 5A**). Moreover, we note that the promoter activity between biological replicates was considerably more variable upon expression of *xre*^{Pp} (**Fig S5A** and **5B**), indicating that the Xre^{Pp}:DNA interaction is unstable in the absence of RES^{Pp}. To assess if the weak repression upon induction of *xre*^{Pp} alone is due to lack of formation of a stable Xre dimer, we expressed and purified the isolated Xre^{Pp} antitoxin with a C-terminal His-tag (Xre$^{Pp}_{CHis6}$) to avoid disturbing the dimerisation interface. Purified Xre$^{Pp}_{CHis6}$ was very prone to aggregation and could not be concentrated above 10 µM, supporting that complex formation contributes to stabilising the antitoxin. Moreover, the mass of purified Xre$^{Pp}_{CHis6}$ antitoxin was determined by SEC-MALS to 22 ± 1 kDa, corresponding to a monomer of Xre^{Pp} (**Fig 5B**). In summary, we conclude that the presence of RES^{Pp} is required for formation of a functional and DNA-binding competent Xre^{Pp} dimer.

333 To further investigate the stability the Xre^{Pp} dimer within the complex, mass photometry (MP), which
334 is a single-particle mass-determination method, was used to determine the mass of the purified Xre-
335 RES^{Pp} complex. The particle distribution was not uniform and at 10 nM we observed two populations
336 of which the larger and most abundant was around ~90 kDa and the smaller was around 76 kDa. At
337 5 nM, the same two populations were observed, but with the smaller MW complex being most
338 abundant, however an additional peak around 50 kDa was also seen. Measuring at 2 nM revealed a
339 mostly homogeneous peak at with 50 kDa, with a trailing tail of larger particles. This concentration
340 dependent change in mass distribution and median masses (87 ± 15 kDa, 76 ± 14 kDa, 54 ± 14 kDa)
341 corresponds roughly to a transition from the 4:2 (103 kDa) complex via a 3:2 (86 kDa) to a 2:2 (69
342 kDa) complex (**Fig 5C**). Together, this suggests that even in presence of RES; the Xre^{Pp} dimer is
343 unstable and that the Xre-RES^{Pp} complex can exist on both 4:2, 3:2, and 2:2 forms. To confirm the
344 existence of the 2:2 complex *in vitro*, we expressed and purified a variant of the Xre-RES^{Pp} complex
345 with a N-terminal His_6-tag on Xre (Xre_{NHis6}-RES^{Pp}), which, based on the crystal structure, should
346 prevent Xre dimerisation. The expressed protein was highly prone to precipitation during purification,
347 consistent with a destabilised Xre^{Pp} dimer that would result in free and unstable Xre^{Pp} monomers as
348 well as a 2:2 complex. This was supported by SEC, which showed two peaks corresponding to the
349 2:2 complex and isolated Xre^{Pp} antitoxin, respectively (**Fig S6A** and **6B**). The successful isolation of
350 a 2:2 complex was further confirmed by mass photometry, where the main protein population at both
351 10 nM and 2 nM exhibited masses of 63 ± 18 kDa (**Fig 5D**).
352
353 As the isolated Xre^{Pp} antitoxin is a monomer and induction of xre^{Pp} alone only weakly represses
354 transcription *in vivo*, we predicted that the isolated 2:2 complex, containing two Xre monomers,
355 would also have reduced DNA affinity. Analysis by high-resolution SEC column of samples
356 containing only S4 DNA, only the 2:2 complex, or 2:2 complex and S4 DNA in ratio of 1:10 showed

357 that the elution volume of the 2:2 complex is not affected by the addition of DNA (**Fig 5E**). This
358 supports that the 2:2 is a non-binding form of the Xre-RES^{Pp} complex and thus a model in which the
359 complex exists in a concentration-dependent equilibrium between non-binding (2:2) and DNA-
360 binding (4:2) forms.
361

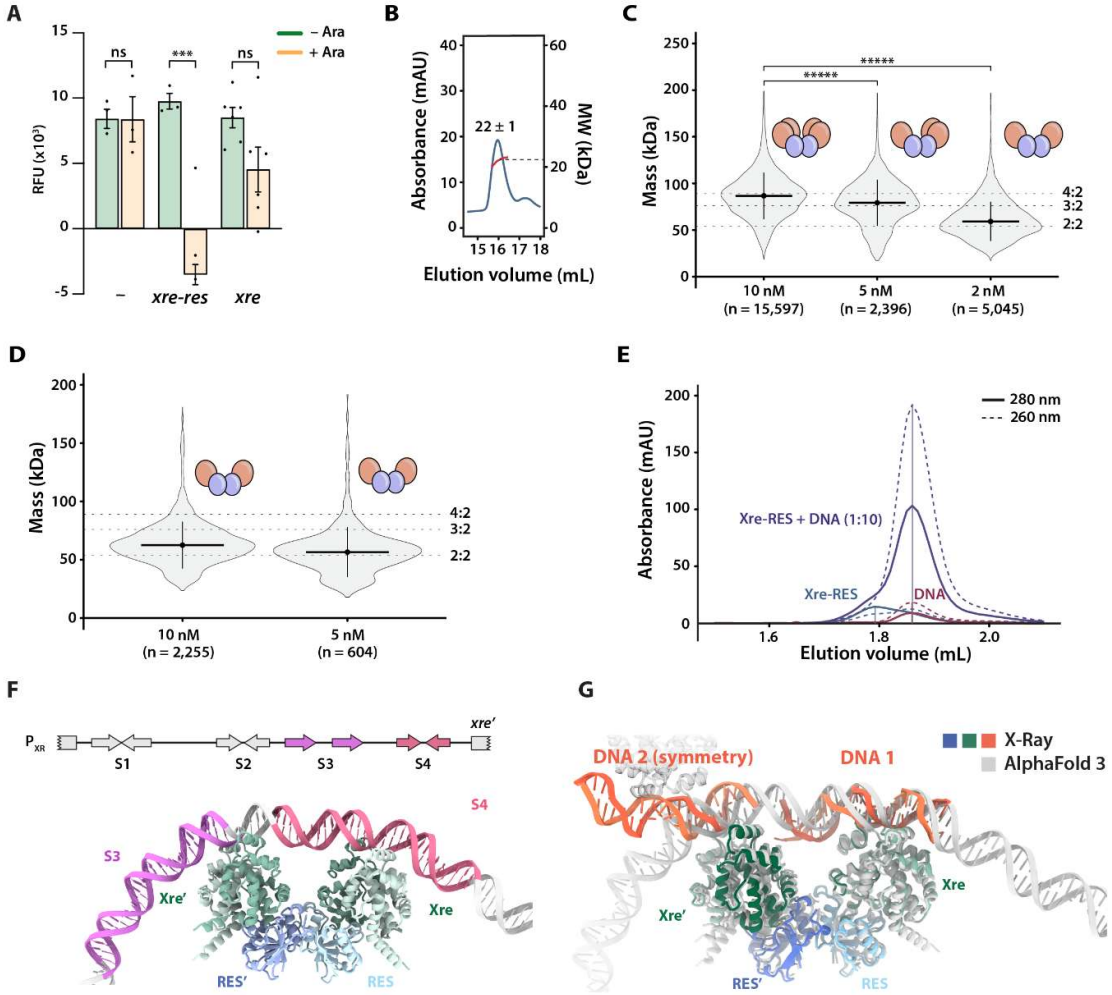

362
363 **Figure 5. DNA binding requires the Xre dimer, which is unstable at low concentrations.**
364 (A) Promoter activity assays in *E. coli* MG1655, where the promoter reporter plasmid pGH254Kgfp::P_{XR}
365 (P_{XR}) was combined with either empty pBAD33 (-), pBAD33::*xre*^{Pp} (*xre*), or pBAD33::*xre-res*^{Pp} vector
366 (*xre-res*), as indicated Complete growth curves and details of the constructs are found in **Fig S4**. Statistical
367 analysis was performed using a two-sample t -test (with equal variances). *ns*, not significant; *, $p < 0.05$.
368 (B) SEC-MALS analysis showing that isolated Xre$^{Pp}_{CHis6}$ is a monomer with an approximate mass of 22 ±
369 1 kDa in solution. The chromatogram shows elution profile measured by 280 nm absorbance (blue) and
370 calculated mass from MALS (red). (C) Single-molecule mass determination of Xre^{Pp}-RES$^{Pp}_{His6}$ at 2, 5, and
371 10 nM. The violin plots represent the density of all measured single-molecule events. The solid black
372 horizontal line indicates the median mass, while the vertical line shows the standard deviation. The

373 theoretical masses of the Xre^{Pp}-RES^{Pp}_{His6} complex with 4:2, 3:2, and 2:2 stoichiometries are indicated by
374 dotted lines. Significance was tested with the Wilcoxon signed rank test. *****, p< 5.55e-7. (D) Single-
375 molecule mass determination for Xre_{His6}-RES^{Pp} on the 2:2 complex form at 2 and 10 nM, as in c. (E) High
376 resolution analytical SEC (a-SEC) analysis of Xre_{NHis6}-RES (Xre-RES, blue), S4 (DNA, red), amd DNA
377 mixed with protein in a 1:10 ratio (Xre-RES + DNA, purple). The full line shows 280 nm absorbance, and
378 the dotted line is 260 nm absorbance. (F) Alphafold3 predicted structure of Xre-RES complex interacting
379 with the full 172 bp promoter region (not all nucleotides shown). (G) Structural alignment of crystal
380 structure of the DNA-bound Xre-RES complex, including the symmetry-related dsDNA molecule
381 (blue/green/orange) with the AlphaFold 3 prediction (grey).
382

383 **Structural basis for Xre-RES^{Pp} binding at two sites in the P_{XR} promoter region**

384 Since the crystal structure suggests that both DNA-binding Xre dimers on a Xre-RES
385 heterohexamer can engage in DNA binding simultaneously, we decided to use Alphafold 3 (AF3) to
386 predict the interaction between Xre-RES and the full 172 bp promoter [29]. The resulting prediction
387 showed high confidence for the Xre-RES protein complex (average pLDDT 90.1), with a more
388 varying confidence for the DNA having pLLDTs between 24.2 and 81.5 (average 53.9). The entire
389 prediction has a PTM score of 0.64 which, while low, is unsurprising given the variance in pLDDT
390 and the length of free DNA. The interaction has an iPTM score of 0.6, which is in the grey zone for
391 confidence and thus would require additional support for validation [29]. This support is provided
392 by comparison to the crystal structure, as the predicted model has both Xre dimers engaged in DNA
393 binding about 20-bp apart (**Fig S7A-C**), with one site closely matching the primary S4 DNA
394 binding site observed in the crystal structure and the other located upstream overlapping partly with
395 S3 as well as involving the region between S3 and S4 (**Fig 5F**). Comparison of the prediction to the
396 crystal structure reveals a good correspondence in the details of the interaction at the primary site,
397 including the central of Arg67 (**Fig S7D**). We consider it, in itself, remarkable that AF3 is able to
398 precisely map the binding site of a bacterial transcription factor within such a long stretch of DNA
399 with nucleotide precision, especially given that there are no structures of similar protein complexes
400 bound to DNA available. However, while the prediction gets the location of the interaction site right
401 and correctly predicts the unusual, asymmetrical way the Xre recognition helices bind the DNA, it
402 does not capture all the subtle details of the deformation of the DNA that take place upon induced

403 fit (**Fig 5F**). Remarkably, however, the predicted interaction of Xre-RES^{Pp} with DNA at the
404 secondary binding site located upstream at the S3-S4 interface is strikingly similar to the interaction
405 to a symmetry-related S4 DNA molecules in the crystal structure. We consider this as strong
406 support for the validity of the overall prediction given the complementarity of the two techniques
407 (**Fig 5G**). The agreement between the crystal structure and the *in silico* prediction suggests that the
408 interaction between the second Xre dimer and the symmetry-related DNA molecules reflect a true
409 biological ability of the complex to interact with higher-order DNA at two sites simultaneously.
410 Collectively, this analysis allows us to put forward a detailed and testable model for how the Xre-
411 RES^{Pp} complex interacts with higher-order promoter DNA via the S3 and S4 repetitive elements.
412

413 **DISCUSSION**

414 In this paper, we present a detailed model for transcriptional autoregulation of the *P. putida xre-res*
415 operon. We show that the heterohexameric Xre-RES^{Pp} protein complex efficiently represses
416 transcription from the *xre-res* locus through direct binding to an imperfect inverted repeat region
417 (S4) in the promoter region, and the structure of the Xre-RES^{Pp} complex bound to this DNA motif
418 provides a detailed molecular view of how the promoter is specifically recognised. We also confirm
419 that the unusual 4:2 stoichiometry of the TA complex observed in the isolated crystal structure [14],
420 in which each of the toxins of a central dimer interacts with a dimer of antitoxins, is present in
421 solution, and further show that isolated Xre^{Pp} antitoxin is a monomer that only weakly represses
422 transcription *in vivo*. This suggests that formation of the Xre dimer, which is stabilised through
423 interactions with the RES toxin, is necessary for efficient binding to DNA. Supportive of this, a 2:2
424 complex present at low concentrations does not bind DNA. Together, these data allow us to propose
425 a model for transcriptional regulation of the *xre-res*^{Pp} operon (**Fig 6**). The expressed 4:2 Xre-RES^{Pp}
426 complex represses transcription through binding via one Xre dimer to the S4 imperfect repeat,
427 followed by binding of the second Xre dimer to the region between S3 and S4. This serves to

428 control transcription and maintain a low cellular concentration of RES toxin. But since the RES-
429 bound Xre-dimer is unstable, dissociation and formation a 2:2 complex will occur over time. In this
430 2:2 complex, Xre still binds to, and neutralises, the RES toxin, but it is unable to bind DNA and
431 consequently, transcription of the *xre-res*^{Pp} operon is eventually reactivated. This increases the
432 cellular concentrations of the Xre antitoxin, leading to the formation of a repressing DNA-binding
433 4:2 complex, possibly via the 3:2 intermediate.
434

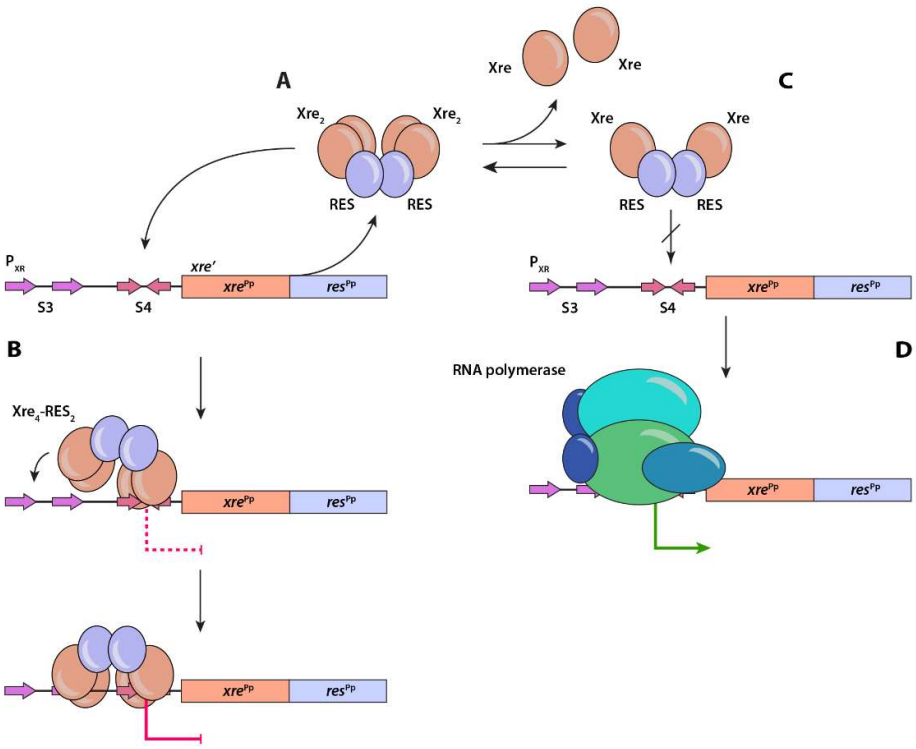

435
436 **Figure 6. Model for transcriptional regulation of the *xre-res*^{Pp} operon**.
437 Expression of *xre-res*^{Pp} leads to the formation of a 4:2 Xre-RES^{Pp} complex (A), in which one Xre dimer
438 binds an imperfect inverted repeat in the promoter region (S4), followed binding of the second Xre dimer
439 to the region between S3 and S4 and subsequently transcriptional repression (B). This lowers the
440 concentration of the Xre antitoxin, leading to the dissociation of the Xre dimer (C) and formation of a toxin-
441 neutralising, but non-DNA binding 2:2 complex (D), and thereby initiation of transcription by the RNA
442 polymerase.
443

444 This model resembles the recently proposed translation-responsive model [30], which states that the
445 expression of TA systems is primarily regulated by the rate of antitoxin production. This model

446 assumes that degradation of antitoxin over time is constant and that the net level of antitoxin thus is
447 controlled by transcriptional and translational activity of the TA operon. Here, we propose that
448 transcriptional autoregulation is based on the concentration of the Xre antitoxin, which again
449 depends on Xre expression from the *xre-res*^{Pp} operon. Interestingly, the structure of a Xre-RES
450 system from *V. parahaemolyticus* (VPA0770-VPA0769) also exists in a heterohexameric (4:2)
451 form that exhibits a W-shaped architecture like Xre-RES^{Pp} and moreover, the antitoxin was also
452 found in an equilibrium between a dimer and a monomer [18]. The VPA0770-VPA0769 complex
453 was found to form a hetero-dodecameric complex (4:8) at high protein concentrations (≥ 5 mg/ml),
454 which was proposed to enhance the stability of the TA complex and thereby facilitate tighter
455 regulation of toxin activity. However, at biologically relevant levels (≤ 1 mg/ml), the complex
456 dissociates into heterohexamers similar to Xre-RES^{Pp}. Additionally, higher-order structural analysis
457 using PISA [31] indicates that the most stable assemblies in solution are either a 2:2 or a 2:4 form.
458 These observations suggest that the *VPA0770-VPA0769* system might operate in a manner similar
459 with the model proposed here. The existence of a dynamic equilibrium between two oligomeric
460 forms of the Xre-RES complex has also been described for the Xre-RES system NatRT from *P.*
461 *aeruginosa* [19], which forms a 4:2 inert state and a 2:1 toxic state and in line with the present
462 findings, the 4:2 NatRT complex autoregulates transcription of *natR-natT*, while the 2:1 state is
463 unable to bind the promoter region and thus repress transcription. However, in this case, the
464 interaction surface between NatR and NatT is mediated by a helix-loop-helix domain (referred to as
465 the 'Flap') not found in RES^{Pp}, and moreover, the switch between the two oligomeric states of
466 NarRT is due to disintegration of the NatT toxin dimer, which we do not observe. Finally, the
467 activity of the NatT toxin affects how the complex binds the promoter, and thus how it regulates
468 transcription. We have not been able to detect NADase activity of RES^{Pp} when bound to Xre,
469 suggesting that the RES domain toxins are regulated and activated by different mechanisms. Taken

470 together, while the details of the mechanisms of Xre-RES systems differ between organisms, the
471 existence of a dynamic equilibrium between oligomeric states, each playing a unique role in activity
472 or regulation of gene expression, appears to apply more generally across Xre-RES homologs.
473
474 The crystal structure of the Xre-RES^{Pp} complex bound to promoter DNA reveals an unusual
475 structural asymmetry in the way the Xre HTH recognition helix interacts with DNA when
476 compared to canonical HTH-containing protein repressors, such as the bacteriophage lambda
477 Cro repressor [20]. This, together with the preference for the imperfect inverted repeat in S4,
478 suggests that asymmetry is an important feature for optimal protein-DNA interaction. We note
479 that the bending of the DNA as well as asymmetrical interaction between Xre and the S4
480 element optimises the involvement of Arg67. The importance of this is supported by the
481 reduced binding affinity observed for Xre-RES^{Pp} towards the 5'-perf and 3'-perf S4 variants
482 *in vitro* (**Table 2**). In addition, the asymmetry of the two recognition helices involved in DNA
483 binding ensures specificity as well as directional binding of the protein complex, positioning
484 the second 'free' Xre dimer to bind a potential secondary operator site. While *in vitro*
485 functional data show that a single Xre-RES^{Pp} complex binds only one copy of S4 dsDNA,
486 deletion of the central palindromic motif of S4 (Δrepeat) within the full P_{XR} promoter,
487 including bases identified by our structural data as critical for specific interaction with Arg67,
488 still results in partial repression by *xre-res*^{Pp} *in vivo*. This finding suggests the existence of a
489 second binding site within the full promoter and supportive of this, the AF3 prediction
490 indicates that the second Xre dimer binds between S3 and S4 in the promoter, in a manner
491 similar to the observed secondary interaction in the crystal. We believe that this interaction is
492 highly significant because crystal contacts often reveal important functional aspects of the
493 crystallised macromolecules. However, these can be hard to validate and separate from mere

494 packing contacts and likewise, hypothetical interactions in predicted models need validation
495 before any conclusions can be drawn. Here, the results of two completely independent
496 techniques (AF3 and x-ray crystallography) strongly support each other in suggesting both the
497 location and specific mode of interaction at the secondary site.
498
499 In conclusion, transcriptional regulation of the *xre-res*^{Pp} operon relies on an asymmetrical
500 interaction of the symmetrical Xre-RES^{Pp} protein complex to the operator site, as well as on a
501 dynamic, concentration-dependent stoichiometry of the Xre-RES^{Pp} complex. Together, this
502 puts forward a detailed and testable model for how bacterial transcription factors interacts
503 with higher-order promoter DNA (**Fig 6**). This model demonstrates how a bacterial protein
504 repressor and its operator sites co-evolve to ensure optimal and specific transcriptional
505 regulation and the presence of two DNA-binding domains allows for a tighter transcriptional
506 repression through avidity, making the system more robust towards both perturbations and
507 mutations.
508
509 **MATERIALS AND METHODS**
510 **Bacterial strains and plasmids**
511 Bacterial strains and plasmids used in this study are listed in **S2 Table**, and DNA oligonucleotides
512 in **S3 Table**. Detailed descriptions of plasmid construction are found in **S1 Text**. For site-directed
513 mutagenesis, the Q5 Site-Directed Mutagenesis Kit from NEB was used according to the protocol
514 and mutagenesis primers were designed using NEBaseChanger.
515
516 **Measurements of promoter activities and *in vivo* repression**

517 For promoter activity assays, *E. coli* MG1655 was co-transformed with transcriptional fusion vector
518 pGH254Kgfp and a pBAD33 vector. Overnight cultures were grown in M9 medium supplemented
519 with 0.2% Casamino acids, 0.4% glycerol, 50 mg/ml chloramphenicol, 25mg/ml kanamycin and
520 0.2% glucose. Overnight cultures were washed once in M9 medium and diluted to 0.03 in M9
521 medium supplemented with 0.2% Casamino acids, 0.4% glycerol, 50 µg/ml chloramphenicol and
522 25µg/ml kanamycin. From this, cultures were split into non-induced or induced (by 0.2% arabinose)
523 sub-cultures. Samples of 200 µl were grown in triplicates in a black/clear bottom 96-well plates
524 (Thermo Scientific, cat. no. 165305), using a Synergy H1 microplate reader (BioTek). Optical
525 density (600 nm) and fluorescence intensity (excitation, 479 nm; emission, 520 nm) was measured
526 every 5 min for 12 h. A strain with empty pGH254Kgfp and pBAD33 was used as control and
527 fluorescence intensity at a specific time point was calculated as described by [32], using the formula
528 $I(t) = I_u(t) - \frac{A(t)}{B(t)} I_b(t)$ where $I(t)$ is the fluorescence intensity at a specific time point, $I_u(t)$ is the
529 uncorrected intensity, $A(t)/B(t)$ is the absorbance ration between the measured culture and the
530 culture used as blank, and $I_b(t)$ is the fluorescence intensity of the culture used as blank. The
531 calculated fluorescent intensity was divided by OD_{600} to obtain corrected fluorescence intensity per
532 OD_{600} unit relative to the control strain (relative fluorescence units, RFU). The assay was repeated
533 three times for each strain. Mean values were calculated for technical triplicates and used to
534 calculate a mean-of-mean values and standard mean of error (SEM) of biological triplicates.
535 Statistical analysis was performed in R using Welch's t-test with the assumption of equal variance.
536 Graphs were prepared with Prism.
537

538 **Protein expression and purification**

539 For protein expression, plasmids pETDuet::res_{NHis6}-xre^{Pp}, pETDuet::xre_{NHis6}-res^{Pp}, or pET-
540 29b(+)::$xre_{CHis6}{}^{Pp}$ were transformed into *E. coli* BL21(DE3). Cells were grown to an OD_{600} of 0.6-

541 0.8, induced by the addition of 0.5 mM IPTG for 20-22 h at 20°C, and harvested by centrifugation
542 (6,000 rpm, 10 min, 4°C).
543
544 For purification of the Xre-RES^{Pp}_{NHis6} and the Xre_{NHis6}-RES^{Pp} complex, cell pellets were
545 resuspended in lysis buffer (50 mM Tris-HCl, pH 8.5, 300 mM KCl, 10 mM imidazole, 3 mM β-
546 mercaptoethanol (BME)) supplemented with 1 ng/µl DNase I and 1 mM phenylmethylsulfonyl
547 fluoride (PMSF). Cells were lysed by high-pressure homogenization (Avestin) at 15,000 psi, and
548 clarified by centrifugation (14,000 rpm, 45 min, 4°C). Clarified cell lysates were loaded onto a 1 ml
549 HisTrap FF column (Cytiva) and columns were washed with lysis buffer including 40 mM
550 imidazole. Protein complexes were eluted with elution buffer (50 mM Tris-HCl, pH 8.5, 150 mM
551 KCl, 300 mM imidazole) and further purified using a 1 ml Source 15Q column (GE Healthcare),
552 running in buffer A (50 mM Tris-HCl, pH 8.5, 5 mM (BME) and a gradient into buffer B (50 mM
553 Tris-HCl, pH 8.5, 5 mM BME, 1 M KCl). Final separation was achieved on a Superdex 200
554 Increase 10/300 GL column (GE Healthcare) equilibrated in gel filtration buffer (20 mM HEPES-
555 KOH, pH 7.5, 150 mM KCl, 5 mM $MgCl_2$, 3 mM BME).
556
557 For purification of Xre alone (Xre_{CHis6}^{Pp}), cell pellets were resuspended in lysis buffer (50 mM
558 HEPES-KOH, pH 7.5, 400 mM KCl, 10 mM imidazole) supplemented with 1 ng/µl DNase I and 1
559 mM PMSF, lysed by high-pressure homogenization (Avestin) at 15,000 psi, and clarified by
560 centrifugation (14,000 rpm, 45 min, 4°C). Clarified cell lysate was loaded onto a 1 ml HisTrap FF
561 column (Cytiva), washed with lysis buffer including 30 mM imidazole and eluted using 300 mM
562 imidazole. Eluate was precipitated overnight at room temperature with 45% ammonium sulphate
563 (AmS) and clarified by centrifugation (20.000 rpm, 30 min, 20° C). Supernatant was collected and
564 further precipitated with 60% AmS overnight. Precipitated protein was collected by centrifugation

565 (20.000 rpm, 30 min, 20° C) and resuspended in gel filtration buffer (20 mM HEPES-KOH, pH 7.5,
566 150 mM KCl, 3 mM BME) until conductivity was 15 mS/cm. Final separation was achieved on a
567 Superdex 75 10/300 GL column (GE Healthcare) equilibrated in gel filtration buffer.
568
569 **Analytical Size Exclusion Chromatography**
570 To screen the interaction between the Xre-RES^{Pp} complex and putative binding sites within the
571 promoter, 30 bp dsDNA oligos corresponding to S1, S2, S3 or S4 in the promoter region (**Fig 1A**
572 and **Fig S1A**) were made using oligos specified in **S3 Table**. Briefly, equimolar amounts of
573 complementary DNA oligos were mixed in milliQ water heated to 95°C and cooling to room
574 temperature. Concentrations were determined by nanodrop, using calculated extinction coefficients,
575 and 1.5 nmoles of dsDNA and/or purified Xre-RES$^{Pp}_{His6}$ each were incubated for 5 min at 37° C.
576 Samples containing protein alone, DNA alone, or mixed protein and DNA were analysed by
577 analytical gel filtration (a-SEC) using a Superdex 200 Increase 10/300 GL column (GE Healthcare)
578 running in DNA binding buffer (20 mM HEPES pH 7.5, 150 mM KCl, 5 mM $MgCl_2$ and 3 mM
579 BME). This method probes only high strength (low K_D) interactions which would be necessary for
580 transcriptional control. To assess stoichiometry of protein to DNA in the interaction, samples with
581 protein to DNA ratios of 2:1, 1:2, and 1:10 were analyzed by a-SEC and SEC-Multi angle light
582 scattering (MALS) in DNA binding buffer. For 1:2 and 1:10 ratios of protein to DNA, a Superdex
583 200 Increase 3.2/300 GL column (GE Healthcare) was used for increased resolution. Data was
584 plotted in R (version 4.3.1) using the Tidyverse package [33].
585
586 **SEC-MALS**
587 For ensemble mass determination, purified protein complex was applied to a size-exclusion column
588 (SEC) coupled to multi angle light scattering (MALS) in DNA binding buffer (20 mM HEPES pH

589 7.5, 150 mM KCl, 5 mM $MgCl_2$, 3 mM BME). For each sample, 20-40 µg was added to a Superose
590 6 increase 10/300 column (GE Healthcare) and MALS spectra was recoded using inline DAWN-
591 HELEOS light scattering and optilab T-rEX refractive index detectors (Wyatt). Mass was
592 determined by analyzing the differential refractive index using the Debye model for proteins
593 integrated in the ASTRA VI software [34]. Data was plotted in R (version 4.3.1) using the
594 Tidyverse package [33].
595
596 **Structure determination**
597 Xre-RES_{Nhis6} and S4 dsDNA mixed in a 2:1 molar ratio with a final protein concentration of 4
598 mg/mL. Triagonal plate-shaped crystals were grown in drops containing 0.1M NA HEPES pH 7.5,
599 10% (w/v) PEG 8000, 8% ethylenglycol, and 0.2 M NaCl. All crystals were cryo-protected in
600 reservoir solution supplemented with 20% (w/v) sucrose and flash frozen in liquid nitrogen prior to
601 data collection. A high-quality diffraction dataset was collected at 0.937Å wavelength on a single
602 crystal cooled to 100 K at the BioMAX beamline at MAX-IV (Lund, Sweden). The dataset was
603 processed with XDS [35] and molecular replacement carried out using PHASER[36]. Model
604 building was done manually in coot with iterative refinement using phenix.refine[37], DNA was
605 built into the model gradually as density became apparent. During the final stages of refinment,
606 phenix.refine was complemented by NAMDINATOR [38] for improved fitting and handling of
607 rotamer outliers. The final model contains 32 chains (24 protein and 8 DNA). Xre is complete in
608 chains B, E, F, H, I, K, N, O, Q, T, W from residues 1-149 (Xre), with chains C and U missing 149,
609 chain R missing 147-149, and chans L and X missing 146-149. All RES proteins were missing the
610 13 N terminal residues from the tag, but were otherwise complete from 1-145 with the exepction of
611 chains A and J which lacks residue 145. DNA chains a and c were built from residue 8-28 (of 30

612 total), b and d from 3-23, e from 7-30, f from 1-24, g from 11-30, and h was from 1-20. The final
613 structure contains, 65 water molecules.
614
615 **Mass photometry**
616 Single molecule mass determination was carried out using the TwoMP mass photometer (Refeyn).
617 Experimental data was acquired through one-minute videos recorded by AcquireMP (ver 2.5)
618 software on precleaned high-precision coverslips with Culterwell gaskets (Grace Biolabs). Focus
619 was automatically found by AcquireMP and was deemed correct when the variance was 0.01. Prior
620 to protein analysis, a mass calibration was performed using Bovine Serum Albumin (BSA) and
621 either Immunoglobulin M (IgM) or α2 macroglobulin (α2M) spanning a mass range of 66 kDa to
622 720 kDa. Standard samples were collected at final concentrations of 10 nM by 10-fold dilution into
623 gel filtration buffer. Collected videos were analyzed in DiscoverMP (ver 2.5) by fitting Gaussian
624 functions to ratiometric contrast values of all events in the video. Mass determination was done by
625 fitting a linear curve between ratiometric contrast and molar mass of standard proteins. The Xre^{Pp}-
626 RES^{Pp} complex was diluted 10-fold, 20-fold, or 40-fold in gel filtration buffer (20 mM HEPES pH
627 7.5, 150 mM KCl, 5 mM $MgCl_2$, 3 mM BME) to achieve final concentrations of 10, 5, and 2 nM,
628 respectively. Videos were collected as with the standards and mass was determined from the
629 calibration curve. Statistical significance was defined using a Bonferroni corrected p value of
630 0.0055, to avoid the multiple comparisons problem. Normality was tested using the Kolmogorov-
631 Smirnov test, and populations were compared using the Wilcoxon test.
632
633 **Isothermal titration calorimetry**
634 Thermodynamic constant determination was carried out using the PEAQ-ITC (Malvern
635 panalytical). Purified protein and dsDNA samples were dialyzed into the DNA binding buffer (20

636 mM HEPES pH 7.5, 150 mM KCl, 5 mM $MgCl_2$, 3 mM BME), after which 20 µM of Xre-
637 RES^{Pp}_{Nhis6} was added to the sample chamber and 300-700 µM dsDNA was titrated in through 13 to
638 17 injections. Each dataset was baseline-corrected by independent measurements of buffer into
639 buffer, titrant into buffer, and buffer into sample. Data analysis was done using Microcal PEAQ-
640 ITC Analysis Software (Malvern panalytical). Data quality was evaluated through minimizing
641 residuals, as well as approximating active concentrations of protein and titrant for fitting to correct
642 N. Reported values are a mean of three independent replicates.
643
644 **Accession codes**
645 Structure factors and coordinates for the Xre-RES^{Pp}:DNA complex structure have been deposited in
646 the Protein Data Bank with PDB ID 9R35.
647
648 **ACKNOWLEDGEMENTS**
649 This work was supported by grants from the Independent Research Fund Denmark (grant 0135-
650 00072B to DEB) and the Novo Nordisk Foundation (grants NNF18OC0030646 and
651 NNF22OC0079855 to DEB). The authors would like to thank Janni Nielsen and Prof. Daniel E.
652 Otzen for help with SEC-MALS, Camilla G. Andersen for help with XRD data analysis, Rasmus
653 Freund for scripts designed to plot the pLDDT and PAE files from the Alphafold3 webserver, and
654 Dr. Kristoffer Winther for help with identification of the four promoter repeat sequences. We also
655 wish to thank Associate professor Magnus Kjærgaard and the MBG Biophysics Core Facility for
656 use of equipment supported by The Carlsberg Foundation. We acknowledge MAX IV Laboratory
657 for time on Beamline BioMAX under Proposal 20220062. Research conducted at MAX IV, a
658 Swedish national user facility, is supported by the Swedish Research council under contract 2018-

659 07152, the Swedish Governmental Agency for Innovation Systems under contract 2018-04969, and
660 Formas under contract 2019-02496.

661

662 **REFERENCES**

663 1. Browning DF, Busby SJ. The regulation of bacterial transcription initiation. Nat Rev
664 Microbiol. 2004;2(1):57-65. doi: 10.1038/nrmicro787. PubMed PMID: 15035009.
665 2. Burgess RR, Travers AA, Dunn JJ, Bautz EK. Factor stimulating transcription by
666 RNA polymerase. Nature. 1969;221(5175):43-6. doi: 10.1038/221043a0. PubMed PMID: 4882047.
667 3. Busby S, Ebright RH. Promoter structure, promoter recognition, and transcription
668 activation in prokaryotes. Cell. 1994;79(5):743-6. doi: 10.1016/0092-8674(94)90063-9. PubMed
669 PMID: 8001112.
670 4. Jacob F, Monod J. Genetic regulatory mechanisms in the synthesis of proteins. J Mol
671 Biol. 1961;3:318-56. doi: 10.1016/s0022-2836(61)80072-7. PubMed PMID: 13718526.
672 5. Aravind L, Anantharaman V, Balaji S, Babu MM, Iyer LM. The many faces of the
673 helix-turn-helix domain: transcription regulation and beyond. FEMS Microbiol Rev.
674 2005;29(2):231-62. doi: 10.1016/j.femsre.2004.12.008. PubMed PMID: 15808743.
675 6. Harrison SC. A structural taxonomy of DNA-binding domains. Nature.
676 1991;353(6346):715-9. Epub 1991/10/24. doi: 10.1038/353715a0. PubMed PMID: 1944532.
677 7. Branden CI, Tooze J. Introduction to Protein Structure: Garland Science; 2012
678 2012/3//.
679 8. Fernandez-Lopez R, Ruiz R, Del Campo I, Gonzalez-Montes L, Boer DR, de la Cruz
680 F, et al. Structural basis of direct and inverted DNA sequence repeat recognition by helix-turn-helix
681 transcription factors. Nucleic Acids Res. 2022;50(20):11938-47. doi: 10.1093/nar/gkac1024.
682 PubMed PMID: 36370103; PubMed Central PMCID: PMCPMC9723621.
683 9. John J, Jabbar J, Badjatia N, Rossi MJ, Lai WKM, Pugh BF. Genome-wide promoter
684 assembly in E. coli measured at single-base resolution. Genome Res. 2022;32(5):878-92. Epub
685 20220428. doi: 10.1101/gr.276544.121. PubMed PMID: 35483960; PubMed Central PMCID:
686 PMCPMC9104697.
687 10. Slattery M, Zhou T, Yang L, Dantas Machado AC, Gordan R, Rohs R. Absence of a
688 simple code: how transcription factors read the genome. Trends Biochem Sci. 2014;39(9):381-99.

689 Epub 20140814. doi: 10.1016/j.tibs.2014.07.002. PubMed PMID: 25129887; PubMed Central
690 PMCID: PMCPMC4149858.
691 11. Makarova KS, Wolf YI, Koonin EV. Comprehensive comparative-genomic analysis
692 of type 2 toxin-antitoxin systems and related mobile stress response systems in prokaryotes.
693 Biology direct. 2009;4:19. Epub 20090603. doi: 10.1186/1745-6150-4-19. PubMed PMID:
694 19493340; PubMed Central PMCID: PMCPMC2701414.
695 12. Freire DM, Gutierrez C, Garza-Garcia A, Grabowska AD, Sala AJ, Ariyachaokun K,
696 et al. An NAD(+) Phosphorylase Toxin Triggers Mycobacterium tuberculosis Cell Death. Mol Cell.
697 2019;73(6):1282-91 e8. Epub 20190218. doi: 10.1016/j.molcel.2019.01.028. PubMed PMID:
698 30792174; PubMed Central PMCID: PMCPMC6436930.
699 13. Piscotta FJ, Jeffrey PD, Link AJ. ParST is a widespread toxin-antitoxin module that
700 targets nucleotide metabolism. Proc Natl Acad Sci U S A. 2019;116(3):826-34. Epub 20181231.
701 doi: 10.1073/pnas.1814633116. PubMed PMID: 30598453; PubMed Central PMCID:
702 PMCPMC6338849.
703 14. Skjerning RB, Senissar M, Winther KS, Gerdes K, Brodersen DE. The RES domain
704 toxins of RES-Xre toxin-antitoxin modules induce cell stasis by degrading NAD+. Mol Microbiol.
705 2019;111(1):221-36. Epub 20181111. doi: 10.1111/mmi.14150. PubMed PMID: 30315706.
706 15. Harms A, Brodersen DE, Mitarai N, Gerdes K. Toxins, Targets, and Triggers: An
707 Overview of Toxin-Antitoxin Biology. Mol Cell. 2018;70(5):768-84. Epub 20180203. doi:
708 10.1016/j.molcel.2018.01.003. PubMed PMID: 29398446.
709 16. Kusumawardhani H, van Dijk D, Hosseini R, de Winde JH. Novel Toxin-Antitoxin
710 Module SlvT-SlvA Regulates Megaplasmid Stability and Incites Solvent Tolerance in
711 Pseudomonas putida S12. Appl Environ Microbiol. 2020;86(13):1-17. Epub 20200617. doi:
712 10.1128/AEM.00686-20. PubMed PMID: 32358012; PubMed Central PMCID: PMCPMC7301842.
713 17. Zhou J, Li S, Li H, Jin Y, Bai F, Cheng Z, et al. Identification of a Toxin-Antitoxin
714 System That Contributes to Persister Formation by Reducing NAD in Pseudomonas aeruginosa.
715 Microorganisms. 2021;9(4). Epub 20210402. doi: 10.3390/microorganisms9040753. PubMed
716 PMID: 33918483; PubMed Central PMCID: PMCPMC8065639.
717 18. Zhang Y, Song X, Chen C, Liu L, Xu Y, Zhang N, et al. Structural insights of the
718 toxin-antitoxin system VPA0770-VPA0769 in Vibrio parahaemolyticus. Int J Biol Macromol.
719 2023;242(Pt 3):124755. Epub 20230508. doi: 10.1016/j.ijbiomac.2023.124755. PubMed PMID:
720 37164131.

721 19. Santi I, Dias Teixeira R, Manfredi P, Hernandez Gonzalez H, Spiess DC, Mas G, et al.
722 Toxin-mediated depletion of NAD and NADP drives persister formation in a human pathogen.
723 EMBO J. 2024;43(21):5211-36. Epub 20240925. doi: 10.1038/s44318-024-00248-5. PubMed
724 PMID: 39322758; PubMed Central PMCID: PMCPMC11535050.
725 20. Brennan RG, Matthews BW. The helix-turn-helix DNA binding motif. J Biol Chem.
726 1989;264(4):1903-6. Epub 1989/02/05. PubMed PMID: 2644244.
727 21. Fraikin N, Goormaghtigh F, Van Melderen L. Type II Toxin-Antitoxin Systems:
728 Evolution and Revolutions. J Bacteriol. 2020;202(7):1-14. Epub 20200311. doi: 10.1128/JB.00763-
729 19. PubMed PMID: 31932311; PubMed Central PMCID: PMCPMC7167474.
730 22. Boggild A, Sofos N, Andersen KR, Feddersen A, Easter AD, Passmore LA, et al. The
731 crystal structure of the intact *E. coli* RelBE toxin-antitoxin complex provides the structural basis for
732 conditional cooperativity. Structure. 2012;20(10):1641-8. Epub 20120913. doi:
733 10.1016/j.str.2012.08.017. PubMed PMID: 22981948; PubMed Central PMCID:
734 PMCPMC3507626.
735 23. Garcia-Pino A, Balasubramanian S, Wyns L, Gazit E, De Greve H, Magnuson RD, et
736 al. Allostery and intrinsic disorder mediate transcription regulation by conditional cooperativity.
737 Cell. 2010;142(1):101-11. Epub 2010/07/07. doi: 10.1016/j.cell.2010.05.039. PubMed PMID:
738 20603017.
739 24. Overgaard M, Borch J, Jorgensen MG, Gerdes K. Messenger RNA interferase RelE
740 controls relBE transcription by conditional cooperativity. Mol Microbiol. 2008;69(4):841-57. Epub
741 20080604. doi: 10.1111/j.1365-2958.2008.06313.x. PubMed PMID: 18532983.
742 25. De Bruyn P, Girardin Y, Loris R. Prokaryote toxin-antitoxin modules: Complex
743 regulation of an unclear function. Protein Sci. 2021;30(6):1103-13. Epub 20210407. doi:
744 10.1002/pro.4071. PubMed PMID: 33786944; PubMed Central PMCID: PMCPMC8138530.
745 26. Cormack BP, Valdivia RH, Falkow S. FACS-optimized mutants of the green
746 fluorescent protein (GFP). Gene. 1996;173(1 Spec No):33-8. doi: 10.1016/0378-1119(95)00685-0.
747 PubMed PMID: 8707053.
748 27. Takeda Y, Folkmanis A, Echols H. Cro regulatory protein specified by bacteriophage
749 lambda. Structure, DNA-binding, and repression of RNA synthesis. J Biol Chem.
750 1977;252(17):6177-83. doi: 10.1016/S0021-9258(17)40047-0. PubMed PMID: 330523.
751 28. Shimon LJW, Harrison SC. The phage 434 OR2/R1-69 complex at 2.5 Å resolution.
752 Journal of Molecular Biology1993. p. 826-38.

753 29. Abramson J, Adler J, Dunger J, Evans R, Green T, Pritzel A, et al. Accurate structure
754 prediction of biomolecular interactions with AlphaFold 3. Nature. 2024;630(8016):493-500. Epub
755 20240508. doi: 10.1038/s41586-024-07487-w. PubMed PMID: 38718835; PubMed Central
756 PMCID: PMCPMC11168924.
757 30. Ramisetty BCM. Regulation of Type II Toxin-Antitoxin Systems: The Translation-
758 Responsive Model. Front Microbiol. 2020;11(May):895. Epub 20200505. doi:
759 10.3389/fmicb.2020.00895. PubMed PMID: 32431690; PubMed Central PMCID:
760 PMCPMC7214741.
761 31. Krissinel E, Henrick K. Inference of macromolecular assemblies from crystalline
762 state. J Mol Biol. 2007;372(3):774-97. Epub 20070513. doi: 10.1016/j.jmb.2007.05.022. PubMed
763 PMID: 17681537.
764 32. Jurenas D, Fraikin N, Goormaghtigh F, De Bruyn P, Vandervelde A, Zedek S, et al.
765 Bistable Expression of a Toxin-Antitoxin System Located in a Cryptic Prophage of Escherichia coli
766 O157:H7. mBio. 2021;12(6):e0294721. Epub 20211130. doi: 10.1128/mBio.02947-21. PubMed
767 PMID: 34844426; PubMed Central PMCID: PMCPMC8630535.
768 33. Wickham H, Averick M, Bryan J, Chang W, McGowan L, François R, et al. Welcome
769 to the Tidyverse. Journal of Open Source Software. 2019;4(43):1686-. doi: 10.21105/joss.01686.
770 34. Edelman J. The low-temperature heat capacity of solid proteins. Biopolymers.
771 1992;32(3):209-18. doi: 10.1002/bip.360320303. PubMed PMID: 1581544.
772 35. Kabsch W. Xds. Acta Crystallogr D Biol Crystallogr. 2010;66(Pt 2):125-32. Epub
773 20100122. doi: 10.1107/S0907444909047337. PubMed PMID: 20124692; PubMed Central
774 PMCID: PMCPMC2815665.
775 36. McCoy AJ, Grosse-Kunstleve RW, Adams PD, Winn MD, Storoni LC, Read RJ.
776 Phaser crystallographic software. J Appl Crystallogr. 2007;40(Pt 4):658-74. Epub 20070713. doi:
777 10.1107/S0021889807021206. PubMed PMID: 19461840; PubMed Central PMCID:
778 PMCPMC2483472.
779 37. Adams PD, Afonine PV, Bunkoczi G, Chen VB, Davis IW, Echols N, et al. PHENIX:
780 a comprehensive Python-based system for macromolecular structure solution. Acta Crystallogr D
781 Biol Crystallogr. 2010;66(Pt 2):213-21. Epub 20100122. doi: 10.1107/S0907444909052925.
782 PubMed PMID: 20124702; PubMed Central PMCID: PMCPMC2815670.
783 38. Kidmose RT, Juhl J, Nissen P, Boesen T, Karlsen JL, Pedersen BP. Namdinator -
784 automatic molecular dynamics flexible fitting of structural models into cryo-EM and

785 crystallography experimental maps. IUCrJ. 2019;6(Pt 4):526-31. Epub 20190627. doi:
786 10.1107/S2052252519007619. PubMed PMID: 31316797; PubMed Central PMCID:
787 PMCPMC6608625.
788
789
790

791 **TABLES**

792 **Table 1**. **Data collection and refinement statistics (molecular replacement).**

	DNA-bound Xre-RES^{Pp} complex (PDB: 9R35)
Data collection	
Space group	P 1 2_1 1
Cell dimensions	
a, *b*, *c* (Å)	81.23, 185.11, 170.79
α, β, γ (°)	90, 90.01, 90
Resolution (Å)	26 – 2.7 (2.77 – 2.70)*
R_{sym} (%)	9.2 (122.7)
$I / \sigma I$	8.29 (0.85)
Completeness (%)	90.3 (83.4)
Redundancy	3.4 (3.0)
CC½ (%)	99.7 (35.8)
Refinement	
Resolution (Å)	26 – 2.7 (2.77 – 2.70)
No. reflections	146,206 (7846)
R_{work} / R_{free} (%)	22.8 (35.2) / 26.9 (36.5)
No. atoms	31,814
Protein	31,524
Solvent	65
Average *B*-factors (Å^2)	
Protein	89.1
Solvent	79.8
RMS deviations from ideal	
Bond lengths (Å)	0.004
Bond angles (°)	0.628
Rotamer (%)	
Favoured	99.6
Outlier	0.4
Ramachandran values (%)	
Favoured	98.1
Allowed	1.5
Outlier	0.4

793 *Values in parentheses represent highest-resolution shell.

794 **Table 2. Isothermal Titration Calorimetry (ITC).**

dsDNA	K_D [M]	SEM	Enthalpy (H) [kJ /mol]	Entropy (-ST) [J/mol]	Free energy (G) [kJ/mol]
S4	$2.31 \cdot 10^{-7}$	$4.61 \cdot 10^{-8}$	-3.35 ± 1.29	-31.8 ± 1.66	-38.4 ± 0.71
5'-perf	$3.41 \cdot 10^{-4}$	$2.64 \cdot 10^{-4}$	-5.36 ± 0.92	-26 ± 2.09	-31.3 ± 1.25
3'-perf	$8.06 \cdot 10^{-5}$	$7.97 \cdot 10^{-5}$	9.14 ± 7.28	-42.9 ± 8.06	-33.8 ± 0.91

795 S4 dsDNA, or variants, was titrated into Xre-RES^{Pp} complex. The calculated binding affinities (K_D), the enthalpy (H), the entropy with
796 temperature (-ST), and the Gibbs free energy (G) are shown. All values are means of three (n=3) independent replicates with standard error
797 of mean (SEM) indicated.
798

799 **SUPPORTIVE INFORMATION**

800 **Fig S1. Determination of the minimal promoter requirements of P_{XR}.**

801 **Fig S2. Functional analysis of the S4 repeat sequence**.

802 **Fig S3. Xre-RES^{Pp} interacts specifically with S4 in a 1:1 protein complex to DNA duplex ratio**.

803 **Fig S4. Crystal structure of the DNA-bound Xre-RES^{Pp} complex.**

804 **Fig S5. Expression of *xre*^{Pp} alone only partially represses transcription from P_{XR}**.

805 **Fig S6. Isolation of the 2:2 Xre-RES^{Pp} complex**.

806 **Fig S7. Alphafold 3 prediction of the interaction between Xre-RES and the full promoter.**

807 **S1 Table. Promoter DNA sequences.**

808 **S2 Table. Strains and plasmids used in this study.**

809 **S3 Tabel. DNA oligonucleotides used in this study**.

810 **S1 Text. Supportive Information Methods.**

811 **S1 Appendix. Source Data for Figures and Tables.**